scientific reports

Check for updates

OPEN

A statistically significant increase in ice supersaturation in the atmosphere in the past 40 years

Charilaos Benetatos[1], Kostas Eleftheratos[1,2]✉, Klaus Gierens[3] & Christos Zerefos[2,4,5,6]

Ice saturation (and supersaturation) is a frequent phenomenon in cold regions of the upper troposphere. Its existence is essential for the formation of ice clouds and a necessary condition for the persistence of contrails. Its spatial and temporal evolution is important for weather and climate. The ice saturation and supersaturation values are found in the upper tail of the probability density function (pdf) of upper tropospheric humidity with respect to ice (UTHi). Here, we analyse the changes in the frequency of occurrence of ice saturation and supersaturation from 1979 to 2020 and compare them to changes in the mean UTHi. Our results show that while the mean UTHi increases near-globally with a rate of about 0.15% per decade, high UTHi values exceeding the 70%, 80%, 90% and 100% thresholds increase faster than the mean, at rates of about 0.7%, 0.6%, 0.4% and 0.3% per decade, respectively. The increasing rates of values found in the upper tail of the UTHi pdf suggest that the ambient conditions for cirrus and contrail formation and persistence will be more favourable in the future and this is expected to further enhance the impact of aviation on climate.

The distribution of water vapour in the upper troposphere and lower stratosphere (UT/LS) is of central importance in several ways: it plays a major role in the balance of planetary radiation; it influences and responds to atmospheric motions and plays a key role in the UT/LS chemistry[1]. In the upper troposphere where temperatures are persistently below −40 °C, it is convenient to express the water vapour concentration as relative humidity with respect to ice (RHi). Based on tropical in situ observations, it has been found that upper tropospheric RHi is close to 100% over convective regions and RHi is often less than 10% in regions with subsidence[2].

The appearance of Ice Supersaturated Regions (ISSRs) is common in the upper troposphere and even occurs in the lowermost stratosphere[3,4]. In these regions, where RHi may exceed 100%, cirrus clouds are potentially formed, and aircraft can produce long-lasting condensation trails (contrails) which may last for up to many hours. Cirrus clouds can affect Earth's radiative balance by modifying the solar and infrared radiation within the atmosphere. Besides naturally formed cirrus clouds, persistent contrails produced by aircraft also affect the radiative budget[5]. Studies show that these contrails contribute to anthropogenic climate change[6,7].

The frequency of occurrence and coverage of natural cirrus and contrails is related to the frequency and degree of ice supersaturation in the UT/LS, which may change in a changing climate even if the mean relative humidity might be constant[8,9], since the distribution of relative humidity (its probability density function) may change.

From a satellite perspective, RHi, a local quantity, is not at hand. Instead, a related quantity, Upper-tropospheric Humidity with respect to ice, UTHi, can be retrieved as a weighted average of RHi profiles in the upper troposphere[10]. UTHi may change in a changing climate either by changes of the underlying RHi profiles or by changes in the weighting function[11]. UTHi can be retrieved from satellite data in the strong water band between about 6 and 7 μm wavelength. Such data are available since 1979 from the series of HIRS instruments on the polar orbiting NOAA and METOP satellites.

Other groups used different types of satellite measurements (e.g. microwave sounders[12]) or even vertically integrated radiosonde profiles (e.g. Köhler et al.[13]) for their investigations. Other global datasets include the free tropospheric humidity (e.g., Brogniez et al.[14,15]), UTH from microwave measurements (e.g., Tsamalis et al.[16]; Gray et al.[17]; Good et al.[18]), and others (e.g. Shi et al.[19]). In this study, we have selected to work with HIRS satellite

[1]Department of Geology and Geoenvironment, National and Kapodistrian University of Athens, Athens 15784, Greece. [2]Biomedical Research Foundation of the Academy of Athens, Soranou Efesiou 4, Athens 11527, Greece. [3]Deutsches Zentrum für Luft- und Raumfahrt, Institut für Physik der Atmosphäre, 82234 Oberpfaffenhofen, Germany. [4]Research Centre for Atmospheric Physics and Climatology, Academy of Athens, Vasilissis Sofias 79, Athens 11521, Greece. [5]Navarino Environmental Observatory (N.E.O), Costa Navarino, Messinia 24001, Greece. [6]Mariolopoulos-Kanaginis Foundation for the Environmental Sciences, Patriarchou Ioakim 30-32, Athens 10675, Greece. ✉email: kelef@geol.uoa.gr

data. We do not say that the HIRS dataset is better than others, but it has some strengths compared to others. The most important one is its length of over 40 years of nearly global coverage. To our knowledge, there is no other dataset with this property. For the quite variable water vapour field, decades-long time series are necessary to detect small trends[20]. Microwave datasets have the advantage of not being sensitive to clouds, but they are less long. Radiosonde data lack homogeneous global coverage, and older ones had too strong errors in the cold upper troposphere. Moreover, different sonde types have different error characteristics. Explicit datasets on ice supersaturation do not exist. Instead, there are many studies in the past looking for various properties of ISSRs, some of them reviewed in Gierens et al.[3]. None of these studies was about the long-term trends.

Over the years, several attempts have been made to produce a continuous data set of UTHi from HIRS satellite data[21–24], but these focussed on the bulk and not on the high tail of the UTHi distribution. The initial methodology was developed by Jackson and Bates[22], based on essential work done by Soden and Bretherton[21]. The algorithm relates UTHi to the brightness temperature in channel 12, T_{12}, and additionally uses T_6, in order to account for different temperature vs. pressure profiles between the tropics and higher latitudes. Shi et al.[25] showed that the T_6 dataset contained a bias due to the increase of the CO_2 concentration, whereas Shi and Bates[23] showed that the T_{12} dataset suffered from a break approximately at the middle of the timeseries due to the switch from HIRS2 to HIRS3/4, which was accompanied by a change in the central wavelength of channel 12 from 6.7 μm to 6.5 μm and a subsequent step change in the measured brightness temperature values. To obtain homogeneous times series of ice supersaturation (that is, in the upper tail of the UTHi distribution) Gierens and Eleftheratos[26] deemed it necessary to reformulate the retrieval and use different coefficients for HIRS2 on one hand, and HIRS3/4 on the other. The homogeneity of time series of UTHi and ice supersaturation has been checked thoroughly for 10° latitude bands, using a statistical breakpoint analysis. Remaining small step changes have been corrected. The applied bias corrections are discussed in the Methods section.

The purpose of this work is to report the observational trends in ice supersaturation in the past 40 years, which is the large-scale humidity environment in which cirrus clouds and contrails form and persist. To our knowledge no other study has examined changes in ice supersaturation over the past 40 years using observational data at a near-global scale. We present the general picture of changes in ice saturation and supersaturation in the recent past, providing possible indications of the likely course of their trends in the near future, which may in turn affect future trends in cirrus and contrails. Note that this is not a dataset of cirrus or contrail occurrence and therefore cannot be used to assess the impact of cirrus and contrails on climate. However, ice supersaturation is the "*conditio sine qua non*" of cirrus and contrails. Thus, if ice supersaturation or its distribution is wrong in models (or not represented at all), one cannot be sure about the modelled distribution, properties, and trends of cirrus and contrails, although their frequency and coverage for present day and the past can be fixed using appropriate satellite data. Satellite simulators that calculate UTHi from the model's humidity profiles should be available for such a purpose, but it might suffice as well to feed these profiles into radiative transfer models and to compute the corresponding brightness temperatures. In this regard, we consider the long-term UTHi and ice supersaturation data, and the knowledge gained from long-term trend analyses, useful for evaluating and validating modern cloud parameterisations, namely those that allow ice supersaturation to occur.

Results

Figure 1 shows the mean UTHi for the 1979–2020 period in 2.5° × 2.5° resolution. The climatology divides the map roughly in three zones. Large UTHi in the tropics, mainly over land (central Africa, west Africa and the Amazon area), the west branch of the Walker circulation, and the Indian Ocean associated with the Madden-Julian oscillation, are probably a signature of deep convection which transports large amounts of water vapour into the upper tropical troposphere. The adjacent subtropical latitude zones are characterised by low UTHi, which reflects the predominant subsidence in these regions. These two features are essential parts of the Hadley cells. The mid-latitudes up to 60° north and south are again characterised by higher UTHi values. Indeed, these are regions where ice supersaturation is a frequent phenomenon.

Trend analysis is performed in the monthly mean UTHi values (Fig. 2) as well as the monthly fraction exceedances of the UTHi above 70, 80, 90 and 100% (Fig. 3). All trends have been estimated from monthly de-seasonalized UTHi data (see Methods). Results show that there is a clear dependence between the mean UTHi anomalies trends and the latitude. At the mid-latitudes (between 30° and 60° N/S), trends are positive, and they exhibit relatively low standard error. It is also observed that trends are increasing as the latitude increases. In the tropics (between 30° S and 30° N) the observed trends are negative except for the area between 0–10° N. Standard error is also relatively low. Therefore, based on the data, for the period between 1979 and 2020 the monthly mean UTHi tends to increase in the midlatitudes and decrease in the tropics. The trends range between −0.19 and 0.51%/decade. The globally averaged trend is about 0.15% per decade, so the near global monthly mean UTHi tends to increase in this period. Statistical significance tests show that the trends are indeed significant at the 99% significance level in all latitude zones except from 20–40°S and 0–30°N.

The trends and their respective statistical significance in the fraction exceedances anomalies above certain thresholds are also explored (Fig. 3). The trends follow the same pattern as in the monthly mean UTHi values, with the high latitude zones exhibiting higher trends than the tropics. Trends seem to be larger than in the mean UTHi values, ranging between 0 and 1.39%/decade for 70%, between 0 and 1.14%/decade for 80%, between −0.01 and 1.27%/decade for 90% and between 0 and 1.04%/decade for 100%.

All trends exhibit relatively low standard error, and they are tested for statistical significance in the 99% confidence level. For the 70 and 80% thresholds, trends are significant except in the 10–20° N/S zones. The trends for the 90 and 100% thresholds are significant except in the 10–20° N and the 0–20° S zones. Near global average trend values are 0.69%/decade for 70%, 0.57%/decade for 80%, 0.43%/decade for 90%, and 0.3%/decade for 100%. The trends decrease with increasing thresholds which implies changes in the distribution of UTHi.

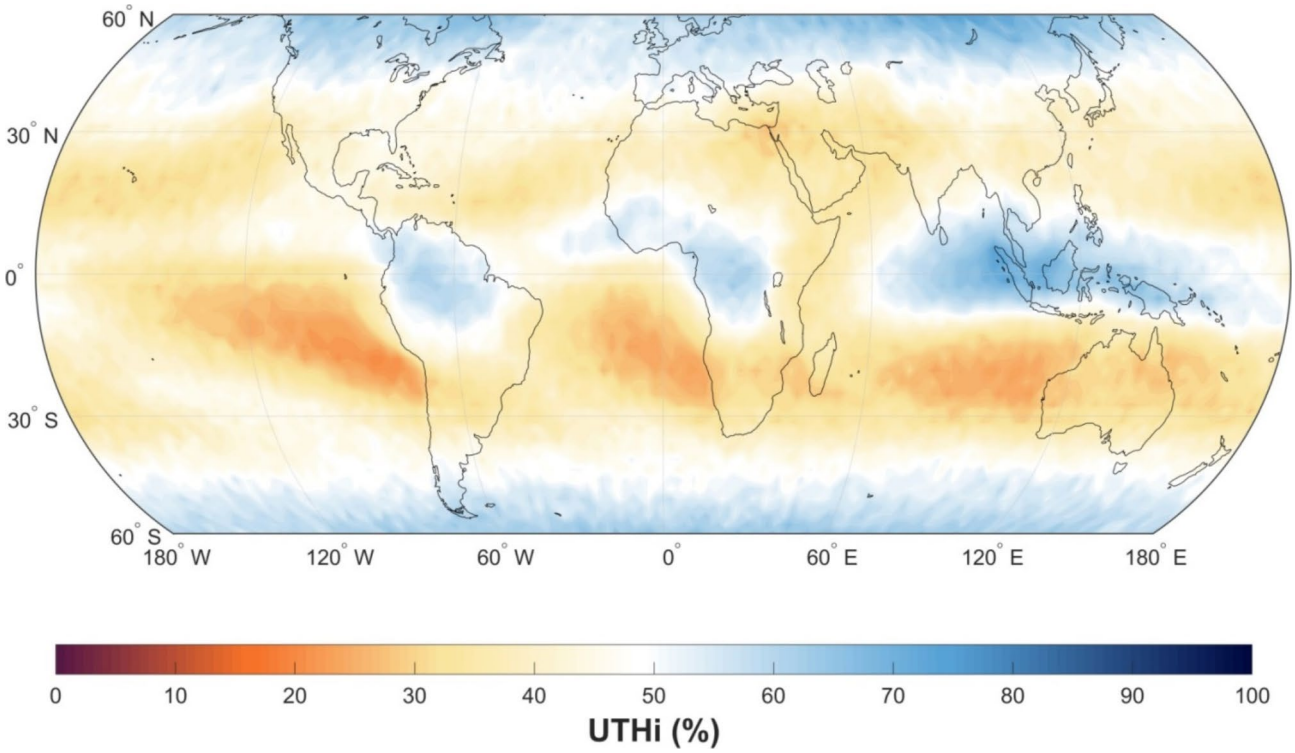

Fig. 1. Mean UTHi over the period from 1979 to 2020. Red (blue) colours demonstrate dry (humid) areas.

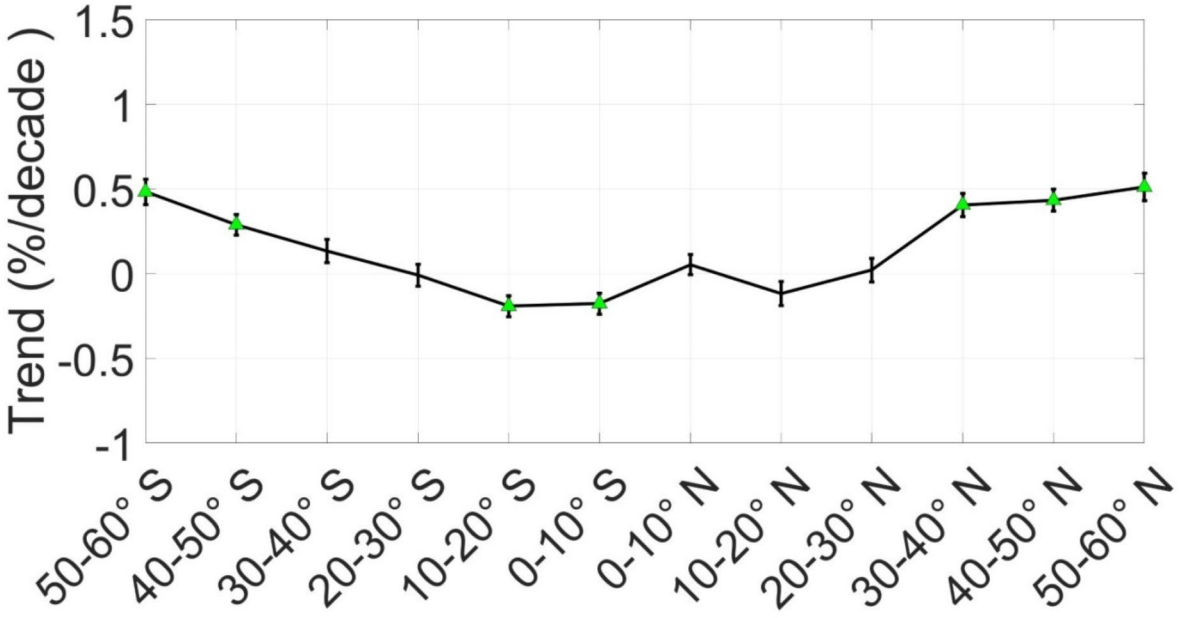

Fig. 2. Trend analysis applied on the monthly mean de-seasonalized anomalies of UTHi. Trends are calculated for the period between 1979–2020. Statistically significant trends ($P < 0.01$, Mann-Kendall trend test) are marked with green triangle symbols.

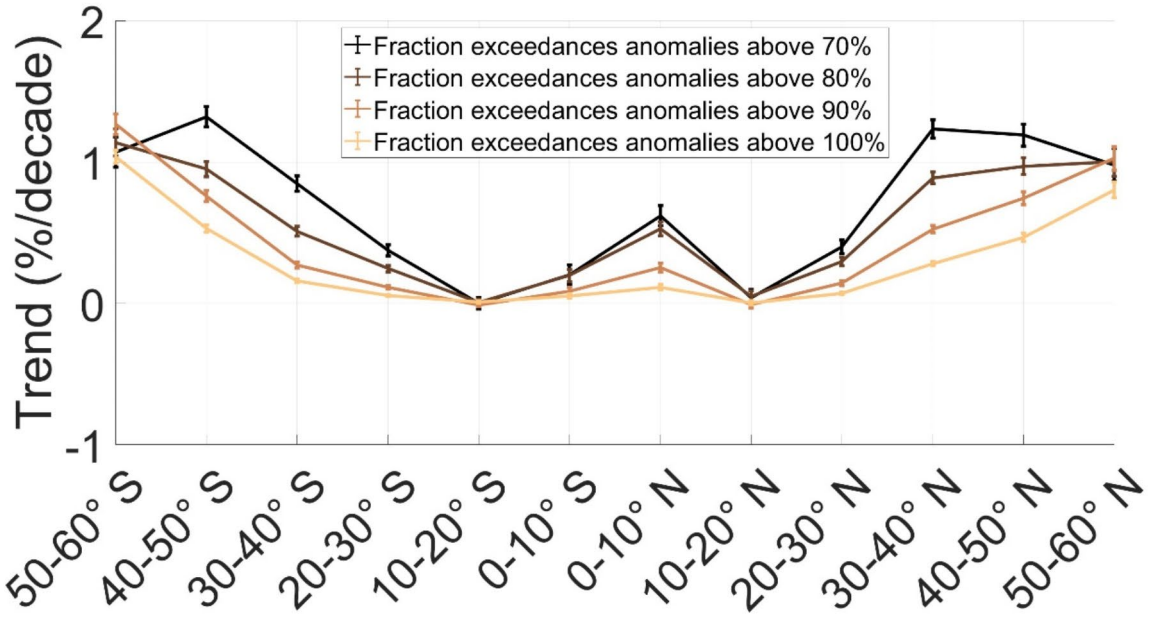

Fig. 3. Trend analysis applied on the monthly mean de-seasonalized anomalies of fraction exceedances of UTHi above 70%, 80%, 90% and 100%. Trends are calculated for the period between 1979–2020.

Trends (% dec^{-1})	Mean UTHi	70% fraction exceedances	80% fraction exceedances	90% fraction exceedances	100% fraction exceedances
50–60°N	**0.51**	**0.98**	**1.00**	**1.03**	**0.80**
40–50°N	**0.43**	**1.19**	**0.97**	**0.75**	**0.47**
30–40°N	**0.41**	**1.23**	**0.89**	**0.53**	**0.28**
20–30°N	0.02	**0.40**	**0.30**	**0.14**	**0.07**
10–20°N	−0.12	0.04	0.05	−0.01	0.00
0–10°N	0.05	**0.62**	**0.53**	**0.25**	**0.11**
0–10°S	**−0.18**	**0.20**	**0.20**	0.08	0.05
10–20°S	**−0.19**	0.00	0.01	−0.01	0.01
20–30°S	−0.01	**0.38**	**0.25**	**0.11**	**0.06**
30–40°S	0.13	**0.85**	**0.51**	**0.27**	**0.16**
40–50°S	**0.29**	**1.32**	**0.95**	**0.76**	**0.53**
50–60°S	**0.48**	**1.07**	**1.14**	**1.27**	**1.04**

Table 1. Trends (% per decade) in UTHi and its fraction exceedances above 70, 80, 90 and 100% for the period between 1979–2020 per 10-degree latitude zone. Bold: statistically significant with $P < 0.01$ according to the Mann-Kendall trend test.

Table 1 summarizes the observed trends in the mean UTHi values and in the values that are found in the upper tail of its probability density function, exceeding 70%, 80%, 90% and 100%.

Discussion

Results from the analysis presented in this paper can be compared to studies similar in nature as the one by Irvine and Shine[27] where they investigated the change in the frequency of Cold Ice Supersaturated (CISS) regions from the 1979–2005 (historical) period to mid-21st century and until the end of it with the help of global climate models. In their study, they conclude that the change of such regions is regional rather than globally uniform. They take a close look at the northern hemisphere polar regions, the mid latitudes as well as the tropical regions which contain the northern and southern parts of the tropics. In the northern polar region, they report an increase in the CISS frequency of 1.7% points by mid-century and 4.9 by the end of the century. In the northern hemisphere midlatitudes there is a small increase in the frequency of the CISS regions of around 0.7 and 0.9% points until the mid-21st century and the end of it, respectively. Some discrepancies are found between the models on the sign of the change. In the tropics, they report a strong decrease in the CISS frequency of 3.3% points by the mid-century and of 8.8 points by the end of the century. On a global scale, they report a multi-

model-mean decrease of CISS frequency from 11% (historical period) to about 7% (end of century). Comparing our trends analysis' results on the fraction exceedances anomalies to the Irvine and Shine research[27], there is agreement in the sense that there is no globally uniform response, and that the high UTHi values tend to increase in the last 40 years in the midlatitudes. Negative trends are not observed in the tropics, at least regarding the monthly mean upper tail UTHi values. Some statistically significant negative trends can be found in the tropics in the mean UTHi values, but no negative trends can be found in the tropics for the upper-tail UTHi values.

Wright et al.[28], investigated the zonal mean relative humidity response between two model simulations. One with 1979 concentrations of greenhouses gases and one with doubled CO_2. Results from their Fig. 1 indicate a distinctive pattern dependent on latitude, where the relative humidity decreases throughout the tropical upper troposphere, subtropics and extratropical free troposphere, with a slightly more noticeable decrease in the Southern Hemisphere. The same figure also shows a reversal of this trend in the midlatitudes. Comparing our findings to this study, there is agreement regarding the general pattern of the response. In our data, mean UTHi values tend to decrease in the tropics. That trend reverses in the midlatitudes and keeps increasing until below the polar regions. There is also a slightly more negative trend in the southern part of the tropics which coincides with their findings.

Likewise, Sherwood et al.[29] used 18 general circulation models comparing the first ten years of simulations to ten years after the CO_2 has doubled. Rate of CO_2 increase is about 1% per year. Specifically, they examined the relative humidity changes divided by the change in global mean sea surface temperature for the same duration to obtain a climate sensitivity of relative humidity. Their results show negative changes in relative humidity in the midlatitude and tropical upper most troposphere. Large increases in relative humidity are estimated around the extratropical tropopause and just above the tropical tropopause, each of which reaches about 2% or more per kelvin of warming. Again, there is a qualitative agreement between our results and the study[29] regarding the observation of negative trends in the tropics and the reversal of the trend as we move to higher latitudes.

We note here that Wright et al.[28] identified changes in circulation and temperature due to a doubling of atmospheric CO_2 as key drivers for the simulated RH changes, while Sherwood et al.[29] reached similar conclusions about the mechanisms that govern global and regional RH changes in a warmer climate. Our results, which are based on observational data, align with and generally support the modelling results. Therefore, some possible physical reasons for the observed trends in mean UTHi can be linked to changes in circulation and temperature due to increased greenhouse gases.

But we must be aware of the difference between relative humidity (a local quantity) on one hand and UTH (a vertical integral of relative humidity) on the other. Two of the authors (Gierens and Eleftheratos[11]) investigated changes in UTH under constant RH. As UTH or UTHi are weighted averages of profiles of RH, there are two possibilities: Either the weighting function that defines UTH changes in a warmer atmosphere or the RH profiles change, or both. The authors showed that, if the distribution of RH remained constant, climate change would modify the weighting functions such that lower UTH would result, in contrast to what the satellite data show. Thus, the distribution of RH cannot be constant, it must shift to higher values far enough to overcompensate the UTH-decreasing effect of the weighting function. This means that as the temperatures rise, the absolute humidity is rising as well, but more than what is needed to compensate for the decrease in RH. Why this is so is not known and has, to our knowledge, never been asked. One possibility is that the temperature increase is stronger in the lower than in the upper troposphere (see Table 1 in Gierens and Eleftheratos[11]). This effect is strong in the extratropics but weak in the tropics, thus consistent with the trends that we find. This could mean that more water vapour than is needed to balance the RH changes can be transported up into the upper troposphere, leading to an increase in upper tropospheric RH in the extratropics and subsequently in the UTH field.

Our results of negative trends in UTHi in most of the tropical regions (Fig. 2) may be linked to changes in the Hadley Circulation (HC) and increasing dryness due to CO_2-induced warming. Lau and Kim[30] analysed model projections from CMIP5 (Coupled Model Intercomparison Project Phase 5) and found robust signals of both strengthening and weakening components of the Hadley Circulation caused by CO_2-induced warming, which drive a pattern of global dryness featuring widespread reduction of tropospheric humidity and increased frequency of dry months, particularly over subtropical and tropical land regions. They report a strengthening of the HC manifested in a "deep-tropics squeeze", i.e., a deepening and narrowing of the convective zone, enhanced ascent, increased high clouds, suppressed low clouds, and a rise of the level of maximum meridional mass outflow in the upper troposphere of the deep tropics. Their study emphasized the physical connection of RH pattern with changes in HC. The anomalous RH pattern stems from the different response rates of moisture convergence and temperature as a function of height and latitude. As a result of CO_2-induced warming, both tropospheric temperature and absolute humidity are increasing everywhere. In the deep tropics, below 400 hPa, RH is enhanced due to strong convection. However, in the layer from 400 hPa to 150 hPa, the RH decreases. This is due to the faster rate of warming in the upper troposphere compared to the lower troposphere, as a result of the moist adiabatic constraint. Here, high RH air transported from below by convection encounters regions of higher temperature in the upper troposphere, resulting in an RH deficit. This RH deficit pattern is further modified by subsidence anomalies associated with changes in HC as discussed in their Fig. 3[30]. According to these findings, it is not surprising that we find decreases in our mean UTHi in most of the tropical regions.

Furthermore, the results of Lau and Kim[30] of increased high clouds in the tropics agree with our results of increasing trends in ice saturation and supersaturation, as the latter are the natural humidity conditions associated with the formation and persistence of cirrus clouds. Decreases in ice supersaturation in the tropics, as reported by Irvine and Shine[27] by the end of the century, do not emerge from our analysis of observational data at least for the period under consideration 1979–2020. We expect the positive trends in ice supersaturation to continue, but we cannot predict with certainty until when or if they will turn negative in the future.

When considering both Figs. 2 and 3, it appears that most of the tropical regions have negative trends in Fig. 2, while the tropical regions in Fig. 3 do not have negative trends. This shows that there is an increasing frequency of high UTHi cases and simultaneously a decrease of the UTHi mean. This obviously means that the probability density function (pdf) of UTHi has changed. To investigate the changes in the pdf of UTHi, Fig. 4 shows the pdfs of UTHi for the northern and southern midlatitudes and the tropics, for the periods 1979–1999 and 2000–2020, and for the whole period 1979–2020. A logarithimic scale is used on the y-axes to highlight the difference between the pdfs in the extreme values (i.e. for UTHi > 70/80/90/100%). Although the shape of the pdf has not changed much from the period 1979–1999 to the period 2000–2020, there appears to be a shift in the pdf toward higher UTHi values and toward fewer lower values, although the latter is not apparent from the logarithmic scale. Why the pdf has changed in the past 40 years and how it will evolve in the future is an open question for future research.

Finally, we briefly mention some things that emerge from this study that other studies have not revealed. The above-mentioned studies are modelling studies based on the output of climate models. Our results are not based on climate simulations but on observational data. Creation of a continuous satellite data set of ice saturation and supersaturation for the last 40 years was not attempted in the modelling studies. The qualitative agreement of our results with the modelling studies reveals that our data support the model results. If there are any discrepancies, they probably point to model deficiencies. Our results focus on both mean UTHi values and values in the high tail of the UTHi distribution. The modelling studies did not analyse long-term observational data of the bulk and the high tail of the UTHi pdf in parallel, as we have done here. Our findings of increasing trends in ice saturation and supersaturation reveal a change in the pdf of UTHi over the past 40 years toward higher UTHi values, as discussed above, that was not revealed by the modelling studies.

Conclusions

To conclude, we have produced a homogeneous timeseries of UTHi values spanning 1979–2020 from HIRS satellite observations. The data are produced by the 2nd order retrieval[26], which was necessary to make the HIRS2/3–4 data consistent not only in the bulk, but also in the upper tail of the distribution. Before the application of the retrieval algorithm, we adjust the T_6 data by removing a false trend related to the increase of the CO_2 concentrations. We also perform a bias correction in the numerator of the UTHi retrieval algorithm to counter apparent jumps around the year 2000. Then we perform a trend analysis on the UTHi data focusing on the mean values as well as on the upper tail of the data. For the mean values, trend analysis shows that estimated trends are about 0.4–0.5% per decade in the northern midlatitudes, between 0.1 and 0.5% per decade in the southern midlatitudes, and that there are negligible or negative trends in the tropics (–0.19 to 0.05%). For the UTHi threshold exceedances in the northern midlatitudes, we observe positive trends of about 0.9 to 1.2%/decade for 70%, 0.9 to 1%/decade for 80%, 0.5 to 1%/decade for 90% and 0.3 to 0.8%/decade for 100% UTHi threshold exceedances values. For the southern midlatitudes we observe positive trends of about 0.8 to 1.3%/decade for 70%, 0.5 to 1.1%/decade for 80%, 0.3 to 1.3%/decade for 90% and 0.2 to 1% for 100% UTHi threshold exceedances values. For the tropics, trends are between 0 and 0.6%/decade for 70%, 0 to 0.5%/decade for 80%, 0 to 0.25%/decade for 90%, and 0 to 0.1%/decade for 100% UTHi threshold exceedances values.

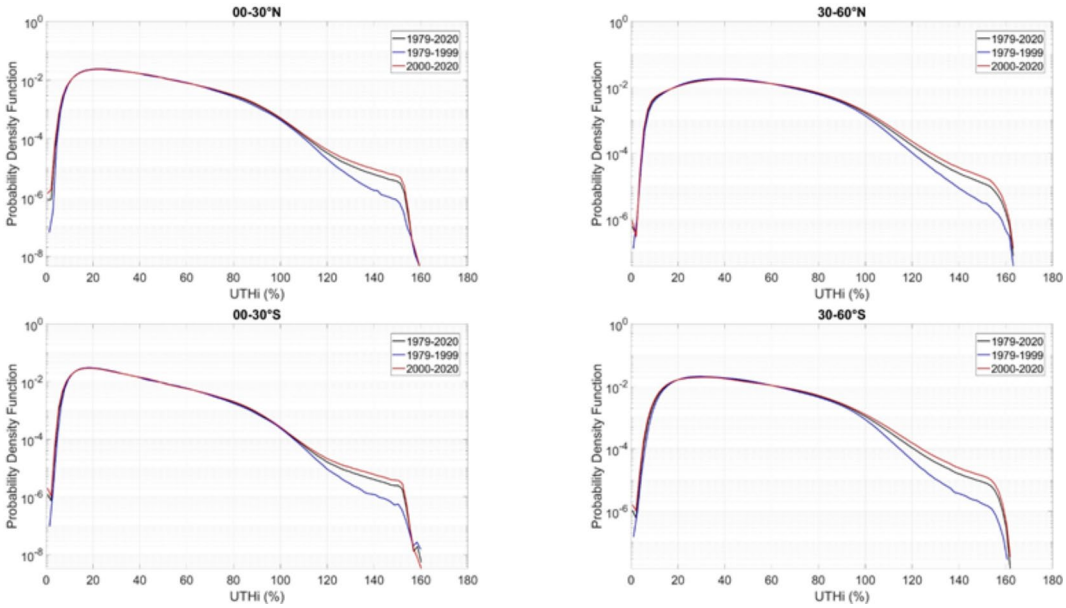

Fig. 4. Change in the probability density function of UTHi in the northern and southern tropics and midlatitudes from the first 20 years (1979–1999, blue lines) to the second 20 years (2000–2020, red lines). Logarithmic scale is used in y-axes. The curves have similar shape, but the pdf of the period 2000–2020 has a longer tail to high and supersaturated values. The black lines show the pdfs for the whole period 1979–2020.

Overall, our results indicate that the mean UTHi is increasing globally with about 0.15% per decade with a latitude-dependent varying trend. This estimate is based on brightness temperature measurements between 1979 and 2020 by the HIRS satellite instruments and therefore our UTHi quantity is a radiance-based quantity. The estimated trend of 0.15% dec^{-1} points to an overall increase in UTHi of about 0.6% in the last 40 years. Our analysis also reveals that the observed statistically significant increasing trends in the midlatitudes are larger for values near or above the ice saturation point than at mean UTHi values, which may have implications in the formation of cirrus and contrails since it is known that the in-situ formation of cirrus clouds via the homogeneous (e.g. Koop et al.[31]) and heterogeneous (e.g. Murray et al.[32]; Hoose and Möhler[33]) nucleation pathways greatly needs ice supersaturation conditions. Analysis of the probability density function (pdf) of UTHi for the northern and southern midlatitudes and the tropics (Fig. 4) indicates that the pdf of UTHi has changed after the year 2000. Although the shape of the pdf has not changed much from the period 1979–1999 to the period 2000–2020, there appears to be a shift in the pdf towards higher UTHi values and fewer lower values. Such a shift implies a large change in the tail of the distribution, meaning that the conditions for in-situ cirrus cloud formation and contrail formation can occur much more often after a slight change in the mean supersaturation. This is expected to be accompanied by changes in cirrus clouds and contrails from aircraft emissions, with implications for climate, however the analysis of the cloud behaviour and the dependence of cirrus cloud trends on ice supersaturation trends is beyond the scope of this study.

Methods

The data used for this study originate from the HIRS instrument onboard the NOAA satellites 6 to 17 and the METOP satellites 02 and 01 ranging between 1979 and 2020. Satellites NOAA 6–14 carried the HIRS2 version of the instrument whereas NOAA 15–17 and METOP 02 and 01 carried the HIRS3 or HIRS4 version. From the HIRS instrument, the brightness temperatures at channels 12 (T_{12}) and 6 (T_6) were retrieved. As the data were produced by HIRS instruments which were onboard different satellites, they could not be mixed directly to produce a homogeneous long time series due to the changes and variations this instrument has undergone over the years. Changes in channel frequencies, filter functions, instantaneous field of view (IGFOV), as well as the switch from HIRS version 2 to HIRS version 3 and 4 are some of the alterations applied to this instrument[24]. The switch from HIRS2 to HIRS3/4 was accompanied by a change in the central wavelength of channel 12 from 6.7 µm to 6.5 µm and a subsequent step change in the measured brightness temperature values with an average discontinuity of about 7 K. HIRS2 data span until July 2005 whereas HIRS3/4 data begin from January 1999. Therefore, between 1999 and 2005 there is an overlap period where both instruments are active. Shi and Bates[23] tried to solve this discontinuity issue between HIRS2 and HIRS3/4 measured T_{12} values by performing inter-satellite calibrations which worked well for the tropics[23,34]. But it turned out that the correction was not good enough in the lower tail of the T_{12} distribution, that is, for high values of UTHi, where a large unphysical trend to higher values was observed in the data[35].

The continuous increase of Carbon dioxide (CO_2) concentrations from approximately 330 ppmv to 410 ppmv between 1979 and 2020, has resulted in a decrease in the brightness temperatures of channel 6 of about 2 K, as simulations show. To account for this false trend, the T_6 values have been corrected with an adjustment that is proportional of the difference between the mean CO_2 concentration in each month and a reference value of our choice (370 ppmv). Details on the procedure of the T_6 data correction are provided in the Supplement Part S1.

Next, the change between the HIRS2 to HIRS3/4 version and the consequent break in the time series needs to be examined. This break in the T_{12} dataset creates a discontinuity in the retrieved UTHi dataset. Gierens and Eleftheratos[26] came up with two sets of coefficients for the T_{12} data, one for HIRS2 and one for HIRS3/4 to counter this issue. Although this removed most of the discontinuity of about 7 K, smaller discontinuities of the order 0.1 K remained, as a breakpoint analysis[36,37] revealed. These small discontinuities have been determined in latitude zones of 5° and after the resulting correction no further breaks are evident. Details are provided in the Supplement Part S2.

The trend estimates presented in Table 1 were determined from linear fits applied to monthly de-seasonalized UTHi data. Data were de-seasonalized by subtracting the long-term monthly mean (1980–2019) pertaining to the same calendar month. Statistical significance of trends was determined by applying the nonparametric Mann-Kendall rank statistic trend test[38] to the de-seasonalized series.

The monthly UTHi data cover the period 1979–2020 and are available on a 2.5° grid from 60° N to 60° S. The spatial resolution of 2.5° is useful to study systematic changes of the humidity conditions that are favourable for cirrus cloud formation on large scales, but apparently, the monthly 2.5° dataset cannot be used for short-term analyses, for example, weather forecasts of cirrus clouds which require high temporal and spatial resolution.

Data availability

Monthly UTHi data and deseasonalized monthly UTHi anomalies analysed in this study, as well as the respective fractions of UTHi threshold exceedances above 70, 80, 90 and 100%, are available in the Zenodo repository, https://zenodo.org/records/13755230.

Received: 24 June 2024; Accepted: 8 October 2024
Published online: 21 October 2024

References

1. SPARC. Assessment of Upper Tropospheric and Stratospheric Water Vapour. D. Kley, J.M. Russell III and C. Phillips (Eds.), (2000). Report No 2, WCCRP No 113, WMO/TD-No 1043.
2. Kley, D. et al. Tropospheric water-vapour and ozone cross-sections in a zonal plane over the central equatorial Pacific Ocean. *Q. J. R Meteorol. Soc.* **123**, 2009–2040 (1997).

3. Gierens, K., Spichtinger, P. & Schumann, U. Ice supersaturation. In: Atmospheric Physics. Background - Methods - Trends, (ed Schumann, U.) Springer, Heidelberg, Germany. 135–150 (2012).
4. Petzold, A. et al. Ice-supersaturated air masses in the northern mid-latitudes from regular in situ observations by passenger aircraft: Vertical distribution, seasonality and tropospheric fingerprint. *Atmos. Chem. Phys.* **20**, 8157–8179 (2020).
5. Kärcher, B. Formation and radiative forcing of contrail cirrus. *Nat. Commun.* **9**, 1824. https://doi.org/10.1038/s41467-018-04068-0 (2018).
6. Lee, D. S. et al. Aviation and global climate change in the 21st century. *Atmos. Environ.* **43**, 3520–3537 (2009).
7. Lee, D. S. et al. The contribution of global aviation to anthropogenic climate forcing for 2000 to 2018. *Atmos. Environ.*, 244 (2021).
8. Manabe, S. & Wetherald, R. Thermal equilibrium of the atmosphere with a given distribution of relative humidity. *J. Atmos. Sci.* **24**, 241–259 (1967).
9. Möller, F. On the influence of changes in the CO2 concentration in air on the radiation balance of the earth's surface and on climate. *J. Geophys. Res.* **68**, 3877–3886 (1963).
10. Gierens, K. & Eleftheratos, K. The contribution and weighting functions of radiative transfer - theory and application to the retrieval of upper-tropospheric humidity. *Meteorol. Z.* **30**, 79–88 (2021).
11. Gierens, K. & Eleftheratos, K. Upper tropospheric humidity changes under constant relative humidity. *Atmos. Chem. Phys.* **16**, 4159–4169 (2016).
12. Lang, T., Buehler, S. A., Burgdorf, M., Hans, I. & John, V. O. A new climate data record of upper-tropospheric humidity from microwave observations. *Sci. Data*. **7**, 218. https://doi.org/10.1038/s41597-020-0560-1 (2020).
13. Köhler, D., Reutter, P. & Spichtinger, P. Relative humidity over ice as a key variable for Northern Hemisphere midlatitude tropopause inversion layers. *Atmos. Chem. Phys.* **24**, 10055–10072. https://doi.org/10.5194/acp-24-10055-2024 (2024).
14. Brogniez, H. & Pierrehumbert, R. T. Using microwave observations to assess large-scale control of the free tropospheric water vapor in the mid-latitudes. *Geophys. Res. Lett.* **33**, L14801. https://doi.org/10.1029/2006GL026240 (2006).
15. Brogniez, H., Roca, R. & Picon, L. A study of the free tropospheric humidity interannual variability using Meteosat data and advection-condensation transport model. *J. Clim.* **22**, 6773–6786. https://doi.org/10.1175/2009JCLI2963.1 (2009).
16. Tsamalis, C. et al. CM SAF Microwave Upper Tropospheric Humidity (UTH) Data Record - Edition 1. Satellite Application Facility on Climate Monitoring. DOI: (2019). https://doi.org/10.5676/EUM_SAF_CM/UTH/V001
17. Gray, R. et al. Upper tropospheric humidity gridded data from 1999 to present derived from satellite observations. Copernicus Climate Change Service (C3S) Climate Data Store (CDS). DOI: (2021). https://doi.org/10.24381/cds.42b801d3
18. Good, E. et al. CM SAF Passive Microwave Upper Tropospheric Humidity (UTH) Data Record - Edition 2. EUMETSAT SAF on Climate Monitoring, DOI: (2024). https://doi.org/10.5676/EUM_SAF_CM/UTH/V002, https://dx.doi.org/10.5676/EUM_SAF_CM/UTH/V002.
19. Shi, L. et al. J. assessing the consistency of satellite-derived upper tropospheric humidity measurements. *Atmos. Meas. Tech.* **15**, 6949–6963. https://doi.org/10.5194/amt-15-6949-2022 (2022).
20. Weatherhead, E. et al. Factors affecting the detection of trends: statistical considerations and applications to environmental data. *J. Geophys. Research: Atmos.* **103**, 17149–17161. https://doi.org/10.1029/98JD00995 (2018).
21. Soden, B. & Bretherton, F. Upper tropospheric relative humidity from the GOES 6:7 μm channel: Method and climatology for July 1987. *J. Geophys. Res.* **98**, 16669–16688 (1993).
22. Jackson, D. L. & Bates, J. J. Upper tropospheric humidity algorithm assessment. *J. Geophys. Res. Atmos.* **106**, 32259–32270 (2001).
23. Shi, L. & Bates, J. J. Three decades of intersatellite-calibrated high-resolution infrared radiation sounder upper tropospheric water vapor. *J. Geophys. Res. Atmos.* **116**, D04108 (2011).
24. Gierens, K., Eleftheratos, K. & Shi, L. Technical note: 30 years of HIRS data of upper tropospheric humidity. *Atmos. Chem. Phys.* **14**, 7533–7541 (2014).
25. Shi, L., Matthews, J. L., Ho, S. P., Yang, Q. & Bates, J. J. Algorithm development of temperature and humidity profile retrievals for long-term HIRS observations. *Remote Sens.* **8** (4), 280 (2016).
26. Gierens, K. & Eleftheratos, K. On the interpretation of upper-tropospheric humidity based on a second-order retrieval from infrared radiances. *Atmos. Chem. Phys.* **19**, 3733–3746 (2019).
27. Irvine, E. A. & Shine, K. P. Ice supersaturation and the potential for contrail formation in a changing climate. *Earth Sys. Dyn.* **6**, 555–568 (2015).
28. Wright, J. S., Sobel, A. & Galewsky, J. Diagnosis of zonal mean relative humidity changes in a warmer climate. *J. Clim.* **23**, 4556–4569 (2010).
29. Sherwood, S. C. et al. Relative humidity changes in a warmer climate. *J. Geophys. Research: Atmos.* **115** (D9). https://doi.org/10.1029/2009JD012585 (2010).
30. Lau, W. K. M. & Lim, K. M. Robust Hadley circulation changes and increasing global dryness due to CO_2 warming from CMIP5 model projections. **112** (12) 3630–3635, (2015). https://doi.org/10.1073/pnas.1418682112
31. Koop, T., Luo, B., Tsias, A. & Peter, T. Water activity as the determinant for homogeneous ice nucleation in aqueous solutions. *Nature*. **406**, 611–614. https://doi.org/10.1038/35020537 (2000).
32. Murray, B. et al. Heterogeneous nucleation of ice particles on glassy aerosols under cirrus conditions. *Nat. Geosci.* **3**, 233–237. https://doi.org/10.1038/ngeo817 (2010).
33. Hoose, C. & Möhler, O. Heterogeneous ice nucleation on atmospheric aerosols: a review of results from laboratory experiments. *Atmos. Chem. Phys.* **12**, 9817–9854. https://doi.org/10.5194/acp-12-9817-2012 (2012).
34. Chung, E. S., Soden, B. J., Huang, X., Shi, L. & John, V. O. An assessment of the consistency between satellite measurements of upper tropospheric water vapor. *J. Geophys. Res.* **121**, 2874–2887 (2016).
35. Gierens, K., Eleftheratos, K. & Sausen, R. Intercalibration between HIRS/2 and HIRS/3 channel 12 based on physical considerations. *Atmos. Meas. Tech.* **11**, 939–948 (2018).
36. Lindau, R. Errors of Atlantic Air-Sea fluxes Derived from Ship observations. *J. Clim.* **16** (4), 783–788. https://doi.org/10.1175/1520-0442_2003_016_0783_eoaasf_2.0.co_2.xml (2003).
37. Lindau, R. & Venema, V. On the multiple breakpoint problem and the number of significant breaks in homogenization of Climate records. *Q. J. Hung. Meteorological Service*. **117** (1), 1–34 (2013).
38. Mitchell, J. M. et al. Climatic change: report of a working group of the Commission for Climatology, Technical Note No. 79, WMO-No. 195. TP. 100, World Meteorological Organization, Geneva, Switzerland, (1966). https://library.wmo.int/records/item/58659-climatic-change (last access: 17 September 2024).

Acknowledgements

The National and Kapodistrian University of Athens, Special Account for Research Grants (KE 17454) for the financial support. The study was partially funded by the AC SAF project of EUMETSAT. The Mariolopoulos-Kanaginis Foundation for the Environmental Sciences. We thank Lei Shi (NOAA NCEI) for providing the HIRS brightness temperature data and for her help and advice when problems occurred.

Author contributions

C.B., K.E., K.G. wrote the main manuscript text, C.B. prepared the figures, C.Z. contributed to methods and

other resources. All authors reviewed the manuscript.

Declarations

Competing interests
The authors declare no competing interests.

Additional information
Supplementary Information The online version contains supplementary material available at https://doi.org/10.1038/s41598-024-75756-9.

Correspondence and requests for materials should be addressed to K.E.

Reprints and permissions information is available at www.nature.com/reprints.

Publisher's note Springer Nature remains neutral with regard to jurisdictional claims in published maps and institutional affiliations.

Supplement to

A statistically significant increase in ice supersaturation in the atmosphere in the past 40 years

Charilaos Benetatos[1], Kostas Eleftheratos ([1,2,]*), Klaus Gierens[3], Christos S. Zerefos[4,2,5,6]

[1] Department of Geology and Geoenvironment, National and Kapodistrian University of Athens, 15784 Athens, Greece
[2] Biomedical Research Foundation of Academy of Athens, Soranou Efesiou 4, 11527 Athens, Greece
[3] Deutsches Zentrum für Luft- und Raumfahrt, Institut für Physik der Atmosphäre, 82234 Oberpfaffenhofen, Germany
[4] Research Centre for Atmospheric Physics and Climatology, Academy of Athens, Vasilissis Sofias 79, 11521 Athens, Greece
[5] Navarino Environmental Observatory (N.E.O), Costa Navarino, 24001 Messinia, Greece
[6] Mariolopoulos-Kanaginis Foundation for the Environmental Sciences, Patriarchou Ioakim 30-32, 10675 Athens, Greece
* corresponding author: Kostas Eleftheratos, kelef@geol.uoa.gr

Part S1. Brightness temperatures corrections at channel 6 (T_6)

To account for the false trend in the T_6 data due to the increased CO_2 concentrations (Shi et al., 2016), the T_6 values have been corrected with the following steps. First, we calculate the ratio of the temperature decrease compared to the CO_2 increase:

$$\frac{\mathrm{d}[T_6]}{d[CO_2]} = \frac{-1.98\ K}{(410-330)\ ppmv} = -0.02475\frac{K}{ppmv}$$

Equation 1

Then we establish a reference value of 370 ppmv and we apply the following correction algorithm in each T_6 value.

$$T_6'(m) = T_6(m) + |-0.02475| * ([CO_2(m) - 370])$$

Equation 2

Where T_6' represents the corrected T_6 values. By applying this formula, the T_6 values are adjusted by a value proportional of the difference between the CO_2 concentration in each month and the reference value of our choice. The correction algorithm is applied on a monthly scale meaning that all T_6 values that fall under the same month are adjusted with the same correction value. Figure S1 shows the T_6 data for the tropics and midlatitudes before and after the corrections due to the CO_2 increase. The left panel (blue lines) shows the false trend in T_6 due to the CO_2 increase and the right panel (red lines) shows the corrected T_6 data where the false trend in T_6 has been corrected.

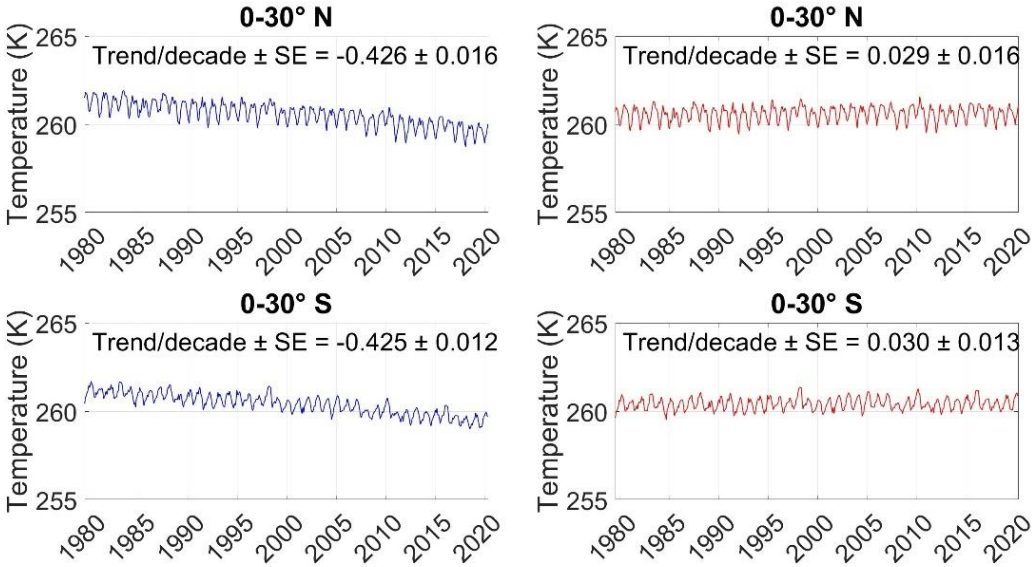

a

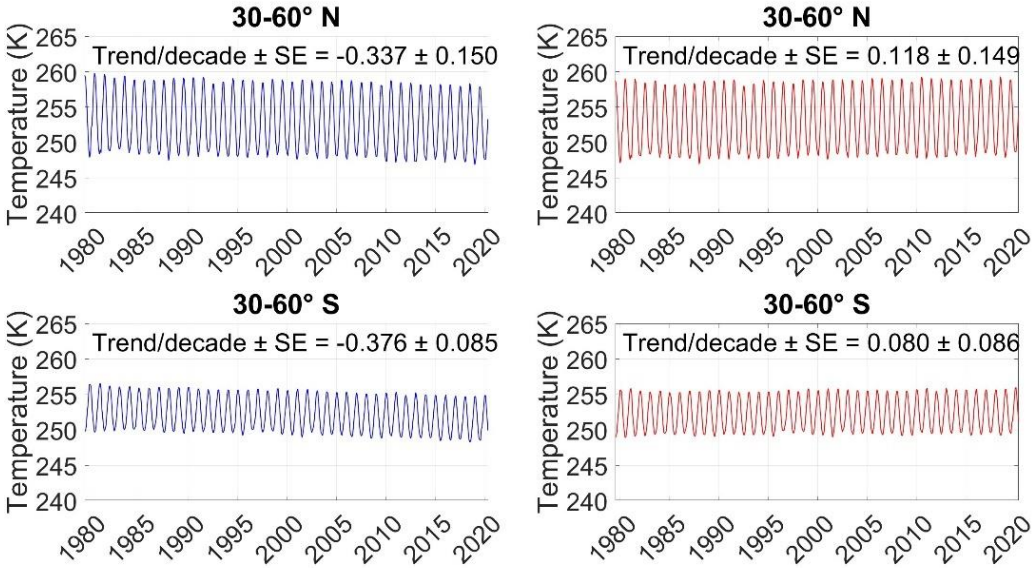

b

Figure S1. T_6 temporal distribution on a monthly scale over 1979–2020 before (left) and after (right) the bias correction due to the CO_2 increase for the tropics (a) and the mid-latitudes (b). Trends per decade ± the standard error are included.

Part S2. Brightness temperatures corrections at channel 12 (T_{12})

A simple bias correction method was followed. First, we calculate the result of the equation $a + b \times T_{12} + c \times T_{12}^2$ for all the point T_{12} data (coefficients a, b, c for HIRS2 and HIRS3/4 T_{12} data are from Table 1 of Gierens and Eleftheratos, 2019). Then we resample this equation result in a 2.5° by 2.5° grid separately for HIRS2 and HIRS3/4. Per 5° of latitude, we estimate a mean value of this equation across all months, and we do the same for HIRS2 and HIRS3/4 grids. Subtracting the HIRS3/4 from the HIRS2 mean value for the same latitude zone we get a correction value that is dependent on latitude. Afterwards, these correction values are added to the HIRS3/4 equation result for all point data. Correction values are provided in Table S1. Then, UTHi is recomputed in monthly, daily, decadal time scales in the 2.5 by 2.5 grid.

In order to test this methodology and compare the datasets before and after the bias corrections, we use a breakpoint analysis based on the calculation of the external variance between two consecutive segments of the UTHi timeseries.

Table S1. Difference of the mean $HIRS_2$ and $HIRS_3$ monthly $a + b \times T_{12} + c \times T_{12}^2$ values per 5-degree latitude range.

	Latitude zone	Difference		Latitude zone	Difference
Northern Hemisphere	55-60°N	–0.0274	Southern Hemisphere	55-60°S	–0.0285
	50-55°N	–0.0344		50-55°S	–0.0214
	45-50°N	–0.0427		45-50°S	–0.0285
	40-45°N	–0.0542		40-45°S	–0.056
	35-40°N	–0.0609		35-40°S	–0.08
	30-35°N	–0.0675		30-35°S	–0.1007
	25-30°N	–0.0924		25-30°S	–0.1065
	20-25°N	–0.1128		20-25°S	–0.1216
	15-20°N	–0.1276		15-20°S	–0.1358
	10-15°N	–0.1235		10-15°S	–0.1319
	5-10°N	–0.0962		5-10°S	–0.1136
	0-5°N	–0.0899		0-5°S	–0.0951

To identify the breaks in a time series we decompose the total variance into external and internal variance. Then, since there is one break in the timeseries that we are aware of (HIRS2 to HIRS3/4 transition) we consider a timeseries with 1 break dividing into 2 segments. Internal variance is the variance inside each one of the segments whereas external variance is the variance between the means of the two segments (Lindau, 2003; Lindau and Venema, 2013). Identifying the maximum external variance, which is the maximum difference in the means of the two segments, can give us information on whether there is a break, as well as where (in which time frame) this break occurs. The relevant algorithm is provided in Eq. 3.

$$\frac{1}{n-1}\sum_{i=1}^{N}\sum_{j=1}^{n_j}\left(x_{ij}-\bar{x}\right)^2 = \frac{1}{n}\sum_{i=1}^{N} n_i(\overline{x_i}-\bar{x})^2 + \frac{1}{n}\sum_{i=1}^{N}\sum_{j=1}^{n_j}\left(x_{ij}-\overline{x_i}\right)^2 + \frac{1}{n(n-1)}\sum_{i=1}^{N}\sum_{j=1}^{n_j}(x_{ij}-\bar{x})^2$$

Equation 3

In Eq. 3, the left side of the equation is the total variance. The right side contains the decomposition of the total variance to the external (left term), the internal (middle term) and a third term, the error of the total mean. Since the last term of a given time series remains a constant then the sum of the external and internal variance is a constant too and it is independent of the number of segments that we separate the timeseries into. The length of the time series is considered as n. It consists of N segments and each of the segments containing n_i members. Single values in the time series are defined as x_{ij}, where i is the segment and j is the place of each value in each segment. The mean of the n_i elements is defined as $\overline{x_i}$ whereas $\bar{x}$ is total mean of the time series (Lindau, 2003; Lindau and Venema, 2013). Calculating the external variance in a loop while dividing it always in two segments for all possible partition combinations of the timeseries and noting each time the external variance, should lead us to the time frame in which the external variance is maximum. For example, the first combination of partitions will separate the time series into two parts. The first part will consist of $n_1 = 1$ values and the second part of $n_2 = n - n_1$ values. In the next iteration the first part will consist of $n_1 = 2$ and

the second part will consist of $n_2 = n - n_1$ and so on. When all iterations are completed then we can identify the period in which the external variance is maximum and therefore there is an evident break in the time series. As an additional validation method, we separate the dataset into time series for each 10 degrees of latitude to see if there is the break is identified in all the latitude zones or just in a few. If the break occurs in all latitude zones and always in the same period which collides with the overlap period (1999–2005) of the HIRS2 to HIRS3/4 transition, then it is possible that there is direct link. We use the monthly averaged data for this analysis.

Afterwards, we apply the breakpoint analysis in the UTHi and the UTHi anomalies before and after the bias correction as was described above. To calculate the UTHi anomalies we de-seasonalize the data by subtracting the long-term (1980-2019) average January, February etc. from each corresponding month. Figure S2 shows the difference in external variance behavior. Mean external variance over all latitudes after the bias correction is significantly smaller and no longer peaks visible between 1999–2005.

The time series of fraction exceedances of UTHi above certain thresholds are also tested with the breakpoint analysis using the external variance as a criterion for the identification of breaks. Fraction exceedances grids are calculated by counting the number of UTHi values that satisfy the condition UTHi >70% (or 80%, 90%, 100%) that fall in a 2.5 by 2.5-degree grid and then dividing by the total number of UTHi values that fall in the same grid. It is important to note that to account for any sub-grid-scale variability and the relatively coarse resolution of the geographical data grid compared to the actual sizes of the ISSRs, it is appropriate to also select UTHi thresholds lower than 100% as others have done when facing the same issue (Irvine and Shine, 2015). The horizontal scale of the data grid is 2.5°x2.5° whereas a typical length of an ISSR is 150 km (Gierens and Spichtinger, 2000). Newer studies about the pathlengths of ISSRs along flight tracks, lead to shorter mean pathlengths (Spichtinger and Leschner, 2016). Fraction of UTHi exceedances have approximately the same behaviour as the mean UTHi values, exhibiting relatively higher external variance around 1999–2005 (the instrumentation change period) before the bias correction. After the bias correction, the external variance no longer exhibits a strong peak around 1999. Figure S3 (a, b, c, d) shows the mean external variance timeseries (which is calculated for each 10° of latitude and then is averaged over) and the respective standard deviation, for the fraction of UTHi exceedances over 70%, 80%, 90% and 100%. Subfigures (b, d, f, h) contain the calculated external variance timeseries for the fraction of UTHi exceedances anomalies for the same threshold values.

The figures show that after the bias corrections, there is no longer a significant break visible in the UTHi time series both in the mean values as well as in the upper tail of the distribution of the data. Given these, we then calculated UTHi on 2.5° × 2.5° data grid for 60°S–60°N on a daily, monthly, and decadal time scale. Finally, trends over the 40-year period are calculated.

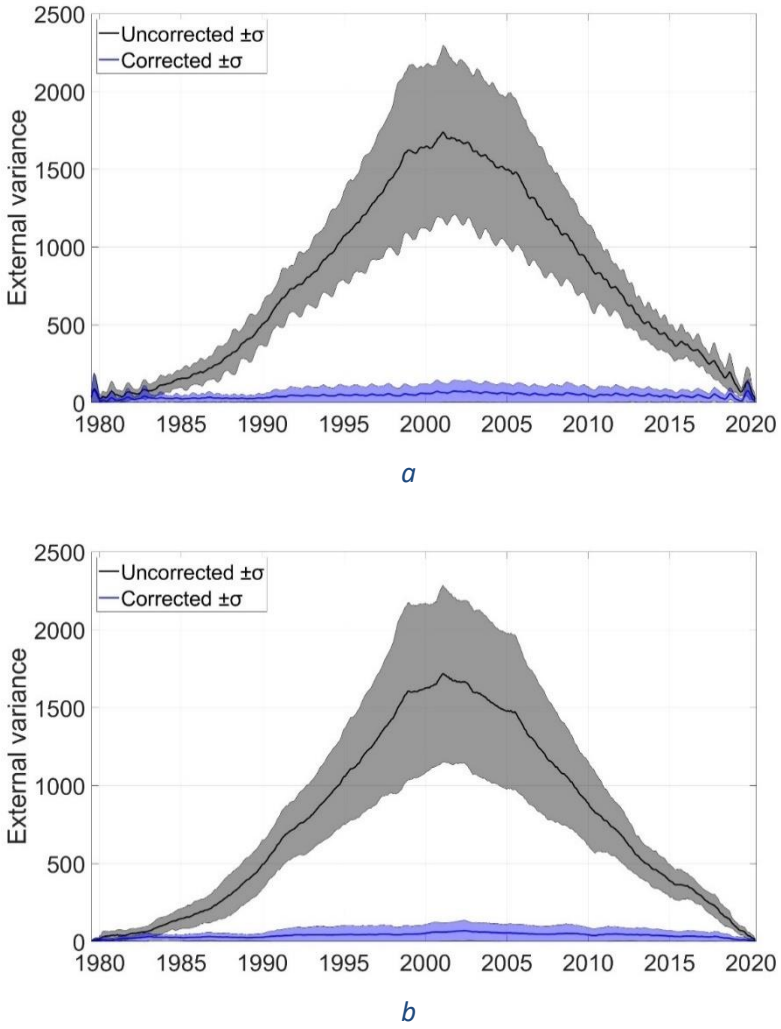

Figure S2. Mean external variance of (a) UTHi and (b) UTHi anomalies across all latitudes (60°N–60°S) ± the respective standard deviation (shade) before (black) and after (blue) the bias correction. The external variance time series is calculated first for each 10° of latitude and then averaged for 60°N–60°S.

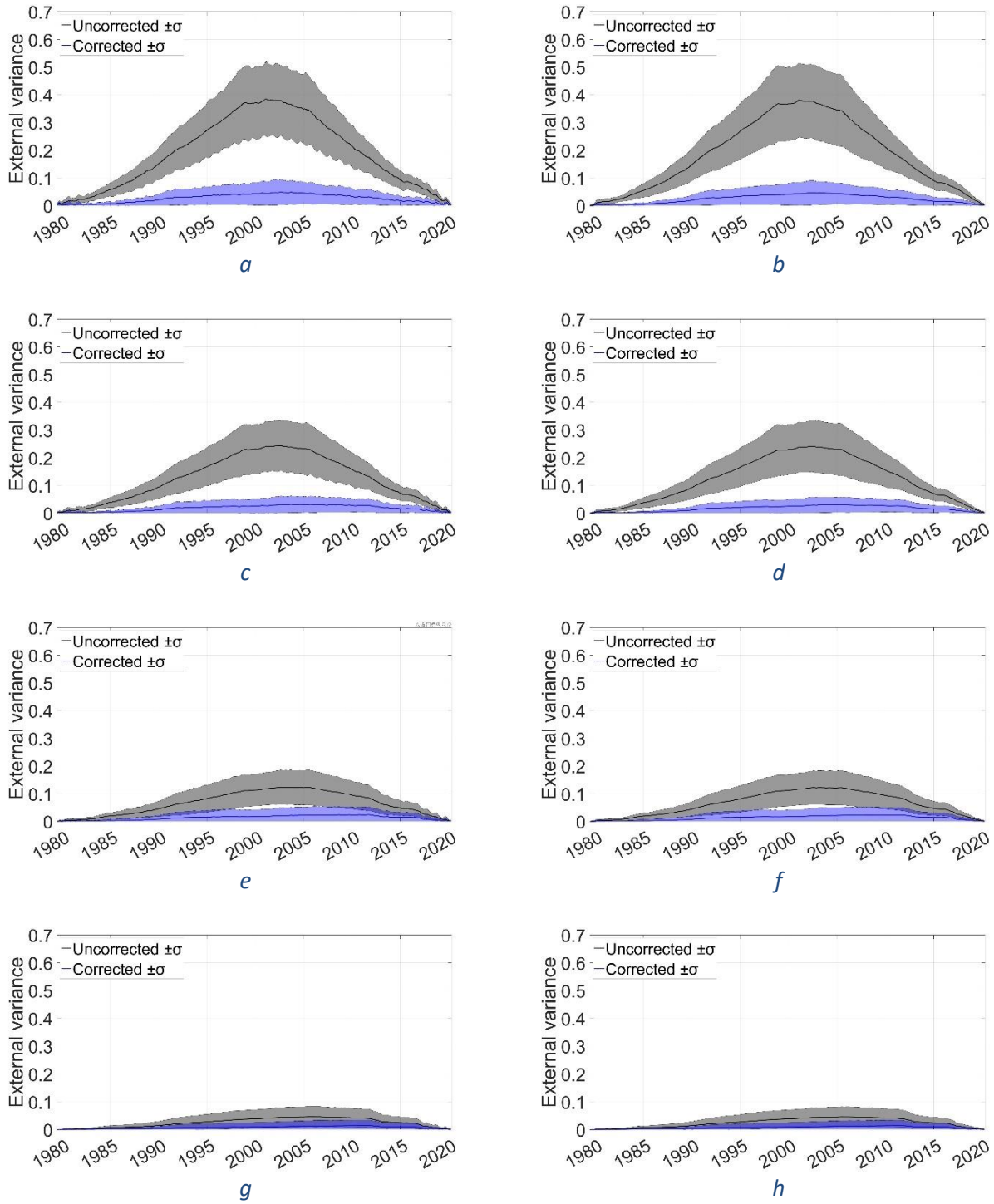

Figure S3. Mean external variance of the fraction of UTHi exceedances above (a) 70%, (c) 80%, (e) 90%, (g) 100% and the respective standard deviation before (black) and after (blue) the bias correction. Subfigures b, d, f, h, show the calculated mean external variance timeseries for the fraction exceedances anomalies of 70%, 80%, 90%, 100% respectively, between 60°N and 60°S and the standard deviation signified with the shady areas. The external variance is calculated first for each 10° of latitude and then averaged for 60°N–60°S.

References

Chung, E.-S., Soden, B., Huang, X., Shi, L., & John, V. An assessment of the consistency between satellite measurements of upper tropospheric water vapor, J. Geophys. Res., 121, 2874–2887, https://doi.org/10.1002/2015JD024496 (2016).

Gierens, K. & Eleftheratos, K. On the interpretation of upper-tropospheric humidity based on a second-order retrieval from infrared radiances, Atmos. Chem. Phys., 19, 3733–3746, https://doi.org/10.5194/acp-19-3733-2019 (2019).

Gierens, K., Eleftheratos, K., & Shi, L. Technical Note: 30 years of HIRS data of upper tropospheric humidity, Atmos. Chem. Phys., 14, 7533–7541, https://doi.org/10.5194/acp-14-7533-2014 (2014).

Gierens, K. & Spichtinger, P. On the size distribution of ice-supersaturated regions in the upper troposphere and lowermost stratosphere, Ann. Geophys., 18, 499–504, https://doi.org/10.1007/s00585-000-0499-7 (2000).

Lindau, R. Errors of Atlantic Air-Sea Fluxes Derived from Ship Observations. J. Climate, 16 (4), 783-788, doi: https://doi.org/10.1175/1520-0442(2003)016<0783:EOAASF>2.0.CO;2 (2003).

Lindau, R. & Venema, V. On the Multiple Breakpoint Problem and the Number of Significant Breaks in Homogenization of Climate Records. Quarterly Journal of the Hungarian Meteorological Service, Vol. 117, No. 1, pp. 1-34 (2013).

Shi, L. Intersatellite Differences of HIRS Longwave Channels Between NOAA-14 and NOAA-15 and Between NOAA-17 and METOP-A, IEEE Transactions on Geoscience and Remote Sensing, vol. 51, no. 3, 1414-1424, doi: 10.1109/TGRS.2012.2216886 (2013).

Shi, L. & Bates, J. Three decades of intersatellite-calibrated High-Resolution Infrared Radiation Sounder upper tropospheric water vapor, J. Geophys. Res., 116, D04108, https://doi.org/10.1029/2010JD014847 (2011).

Shi, L., Matthews, J., Ho, S., Yang, Q., & Bates, J. Algorithm development of temperature and humidity profile retrievals for long–term HIRS observations, Remote Sens., 8, 280, https://doi.org/10.3390/rs8040280 (2016).

Spichtinger, P., and Leschner, M. Horizontal scales of ice-supersaturated regions. Tellus B: Chemical and Physical Meteorology, 68, 29020, doi:10.3402/tellusb.v68.29020 (2016).